Improved emitter performance of RIE black silicon through the application of in-situ oxidation during POCl$_3$ diffusion

Tsun Hang Fung [a],[*], Toni P. Pasanen [b], Yu Zhang [a], Anastasia Soeriyadi [a], Ville Vähänissi [b], Giuseppe Scardera [a], David Payne [c], Hele Savin [b], Malcolm Abbott [a]

[a] *School of Photovoltaic and Renewable Energy Engineering, University of New South Wales, Kensington, NSW, 2052, Australia*
[b] *Department of Electronics and Nanoenegineering, Aalto University, Tietotie 3, 02150, Expoo, Finland*
[c] *School of Engineering, Macquarie University, NSW, 2109, Australia*

ARTICLE INFO

ABSTRACT

Nano-texture has the potential to reduce the optical losses of crystalline silicon solar cells. RIE fabricated black silicon enables near zero reflectance across a broad range of wavelengths and the angular dependence has been shown to be superior to existing technologies. However, in front-contact cells which are the current industrial mainstream architecture, the emitter is located on the front textured side and is typically realized by POCl$_3$ diffusion. The interaction of this process with the nano-texture is complex, which makes it challenging to optimise the electrical performance of the phosphorus emitter. This paper studies the impact of in-situ oxidation during emitter formation to the electrical performance of a POCl$_3$ diffused RIE nanotextured emitter surface. Additional corona charge was applied on the ALD SiO$_2$/Al$_2$O$_3$ stack to avoid the limitation on the emitter performance due to non-ideal surface passivation conditions. After saturation with surface charge, the results demonstrate in-situ oxidation to be an effective technique to improve the electrical performance. An emitter recombination factor of 147 fA/cm^2 was achieved for a 127 Ω/□ emitter formed on reactive-ion etched sample with surface area enhancement factor and effective slope index of 4.19 and 1.63, respectively. Further paths for improvement are identified, particularly relating to the collection of carriers generated by short wavelength light and how that relates to the shape of the texture used.

1. Introduction

In recent years, nano-scaled texturing has been used to reduce the optical loss of c-Si solar cells resulting in improved cell efficiency [1,2]. For example, RIE based texturing has been applied to large area mc-Si front junction solar cells to achieve world record results [3,4]. Furthermore, a shallower form of black silicon formed via chemical etching has been used to address manufacturing problems related to diamond wire sawing [5], to improve cell efficiency [6] and has become standard in production lines [7]. However, to integrate these types of textures with front junction solar cells, the size and shape of the features tend to be compromised to balance the optical and electrical performance, an approach that has been applied to RIE formed textures in numerous works [8–11]. To further improve the cell efficiency it would be beneficial to integrate black silicon textures into solar cells without the need to compromise the near-zero broadband reflectance that has been achieved [12–14]. Whilst these textures have been used

successfully on rear junction cells [2], their integration into the more standard cell architectures has been difficult.

The initial challenge was to develop a technique to passivate large surface area, heavily n-type diffused silicon, since traditional PECVD based depositions of SiN$_x$ were considered incompatible with such extreme surface features [15,16]. A solution to this was found in the form of a positively charged SiO$_2$/Al$_2$O$_3$ stack deposited by atomic layer deposition (ALD) [17]. However, initial attempts at integration into a front junction cell resulted in relatively high emitter recombination due to the presence of excess phosphorous in the emitter region [18]. That work concluded that to achieve further improvements it would be necessary to reduce the phosphorous concentration, thus enabling less recombination and better field effect passivation at the surface.

In-situ oxidation during thermal diffusion has previously been demonstrated as a technique to improve the electrical quality of an emitter region on samples textured with upright random pyramids [19, 20]. The increased flow of oxygen compared to a more traditional

---

* Corresponding author.
E-mail address: tsun.fung@unsw.edu.au (T.H. Fung).

process was found to limit the flux of phosphorous atoms into the silicon, thus reducing the overall dopant concentration and reducing the surface concentration. The benefits of reducing the amount of phosphorous within a solar cell emitter has been demonstrated by many good studies [21,22]. The enhanced surface area to volume ratio of black silicon presents an additional complication when optimising the diffusion process. Previous studies have demonstrated an enhancement in doping concentration, attributed to the enhanced surface area and a likely increased reaction between silicon and PSG [8,10,11,17,23–25], however in some cases the enhancements were marginal [8,24]. An example of strong enhancement was observed for a previous attempt to produce RIE textured selective emitter cells which unintentionally resulted in an emitter with R_{sh} of 40 $\Omega/\square$ (rather than the target of 100 $\Omega/\square$) due to the deep nano-features on the surface [26]. Such results indicate the need for a systematic approach to optimise the POCl$_3$ doping process for extreme black silicon samples.

In this work we address that limitation by applying known high efficiency cell processing techniques to reduce the amount of doping within the emitter. Specifically, we systematically study the effects of in-situ oxidation during thermal diffusion on the quality of P emitters formed on RIE produced ~1 μm tall upright needles with an effective slope index of 1.63, which is about 4 times higher than random upright-pyramid. The electrical characterisation includes the first demonstration on black silicon of the application of a photoluminescence-based technique to measure the emitter collection efficiency. With the reduction in surface concentration achieved we then apply positive corona charge to the surface atomic layer deposited films and demonstrate its ability to further improve the performance. The results demonstrate the lowest recombination P emitters ever achieved on this type of texture and have implications for other types of textures that incorporate nano-scale features.

2. Material and methods

2.1. Fabrication

The process flow of this work is outlined in Fig. 1. A batch of 250 μm thick, double-sided polished 4-inch p-type float zone (FZ) silicon wafers with 1 Ω cm base resistivity was used for RIE texturing. The b-Si nanostructure was fabricated using a process described in Ref. [14] with

an Oxford Instruments Plasmalab 100. The wafers were subsequently cleaned with the standard cleaning procedure [27]. Random pyramid samples were acquired through industry. The random pyramid samples were made on diamond-wire sawed 6-inch p-type mono-Si with a 1.6 Ω cm base resistivity and a thickness of ~180 μm.

POCl$_3$ diffusion was done using a Tempress tube furnace and the recipes were based on those described in Ref. [20]. Random pyramid samples and nanotextured samples were diffused in separate runs due to the differences in wafer dimensions. Polished control samples were loaded in the same run as the nanotextured samples. Pre-deposition for all samples was done at 795 °C for 25 min with a fixed POCl$_3$/O$_2$ ratio = 450/600. Prior to the drive-in step, the temperature was ramped to 855 °C with a fixed ramp rate of 10 °C/minute and a fixed O$_2$ concentration of 8.33% v/v. The drive-in step was done at 855 °C for 30 min with a fixed total nitrogen gas flow of 7.25 slm. The oxygen gas flow was varied to reach the specified O$_2$ concentration (v/v). For more details, see Ref. [20].

Nanotextured and polished samples were passivated with a SiO$_2$/Al$_2$O$_3$ stack deposited with a Beneq TFS-500. Prior to ALD deposition, a 30 s hydrofluoric acid (HF) dip (1%) was used to remove the native oxide on the surface. A SiO$_2$ layer (n = 1.49 at 633 nm, thickness = 20 nm) was first deposited by plasma-enhanced ALD at 200 °C using 120 cycles of oxygen and a commercial silicon precursor. Subsequently, an Al$_2$O$_3$ layer (n = 1.62 at 633 nm, thickness = 33 nm) was deposited at the same temperature by a thermal ALD process consisting of 270 cycles of H$_2$O and TMA precursors. The Al$_2$O$_3$ deposition was performed in the same chamber with the first run without breaking the vacuum in between. During every cycle, a double-pulse of each precursor was used to ensure conformal deposition on the entire deep-RIE surfaces. After ALD deposition, the samples were annealed at 425 °C for 30 min in nitrogen ambient to activate surface passivation [18]. Contactless capacitance-voltage measurements were done on an n-type non-diffused polished reference sample passivated with the same ALD stack. The fixed charge density (Q$_f$) and interfacial trap density (D$_{it}$) was extracted to be 2×10^{11} cm^{-2}eV^{-1} and 3×10^{11} cm^{-2}, respectively.

Random pyramid samples were passivated with SiN$_x$:H (n = 2.08, thickness = 75 nm) deposited by a Meyer Burger MAIA remote plasma enhanced chemical vapour deposition (PECVD) tool at 400 °C [28]. The samples were subsequently fired on a belt furnace with a peak temperature of 740 °C.
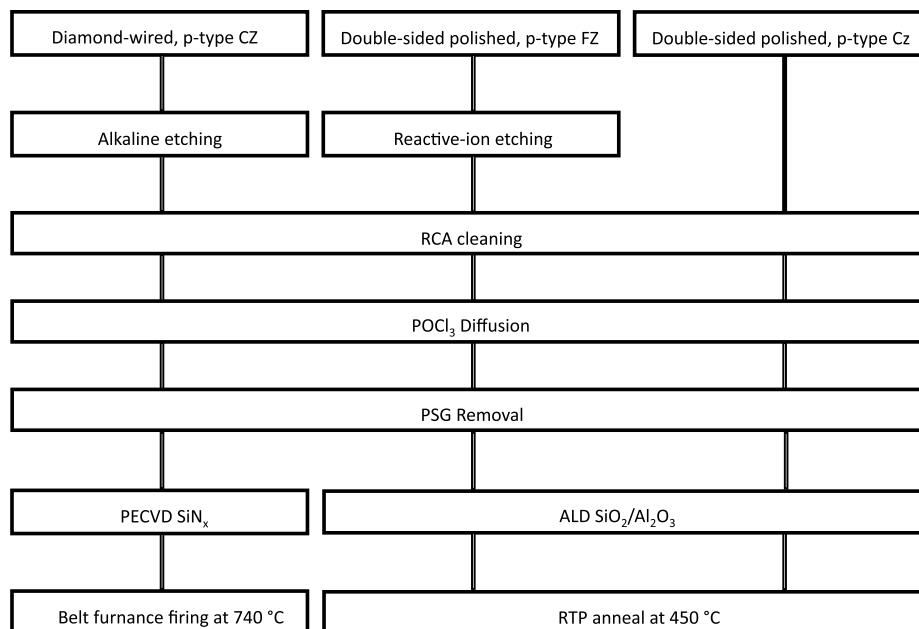

Fig. 1. Process flow chart for random pyramid sample, reactive-ion etched sample and polished reference sample.

2.2. Characterization

SEM images were measured by using a FEI Nova NanoSEM 450. AFM scans were performed by using a Bruker ICON in tapping-mode with 512 line scans. A diamond-like carbon coated silicon probe (TESPD) with a nominal tip radius of 18 nm was used for the random pyramid sample. A minimum 5:1 high-aspect ratio probe (TESPA-HAR) with a nominal tip radius of 10 nm was used specifically for the nanotextured samples. The sampling interval for the random pyramid sample was 78 nm, while the sampling interval for the nanotextured sample was 19 nm. The front surface reflectance of all samples was measured using a commercial spectrophotometer (PerkinElmer 1050) with an integrating sphere.

The sheet resistance was measured by a 4 point-probe scanner (Sunlab Sherescan). The difference in sheet resistance measured between both forward and reverse current direction for all samples was less than 1 $\Omega/\square$. For random pyramid samples, the sheet resistance was measured at 9 points, whilst only the centre point was measured on nanotextured samples to avoid excessive damage of fragile nano-scale features.

The defect density, fixed charge density and surface potential were measured by a Semilab PV-2000A instrument following the standard analysis procedures [29]. A Semilab LCC-300 linear corona charger was used to generate corona charges on the wafer surface for studying the field-effect passivation. After corona charging, the surface potential of the samples was immediately measured every 5 mm across the whole wafer by Semilab PV-2000A using Kelvin probe. The uniformity of the inspected area was confirmed by surface voltage maps. The effective minority carrier lifetime of all samples was measured by quasi-steady-state photo-conductance (QSSPC) via the generalised technique using Sinton WCT-120 [30]. Auger recombination was corrected by using the Richter model [31]. The emitter recombination factor was extracted by the Kane & Swanson method at an injection level of $1–2 \times 10^{16}$ cm^{-3}. The emitter recombination factor (J_{0e}) was monitored by an ex-situ carrier lifetime measurement done between each step of corona charging.

The quantum efficiency of the samples was measured by a photoluminescence-based spectro-response (PL-SR) method [32,33]. Prior to the measurement, a calibrated photo-diode was placed at the sample position to calibrate the photon-flux from the LED array at different wavelengths. This calibration was used for a fixed photo-diode that was placed next to the samples. During the measument, the intesity of the LED array was adjusted to obtain a constant PL signal for all wavelengths in order to avoid the possibility of injection dependent quantum efficiency at low injection. The wavelength-dependent photoluminescence quantum efficiency (PL$_{QE}$) was normalised to the value at 660 nm.

2.3. Calculations

The surface characteristics were extracted from the measured AFM data using the Gwyddion software [34]. The root-mean squared roughness (σ_{rms}) and surface-area-to-projected-area ratio (f_{surf}) were extracted based on the standard definition. The correlation length (τ_L) was extracted by first plotting the data from the AFM scans using a built-in Auto-Correlation Function (G(x)) in Gwyddion. Then, the G(x) was fitted by the equation:

$$G(x) = \sigma_{rms}^2 \exp\left(-\frac{x^2}{\tau_L^2}\right) + g_o \tag{1}$$

where σ_{rms} is the root-mean squared roughness, x is the horizontal distance, τ_L is the correlation length and g_o is a vertical offset to account for the fact that G(x) could drop below zero for coarse surfaces. Facet angles were extracted by local plane fitting over 2 pixels. The facet angle and surface area were both extracted by using the built-in algorithm provided in Gwyddion. No additional image processing was used except for

levelling the data by mean plane subtraction.

The emitter recombination factor (J_{0e}) was extracted by the Kane & Swanson method using the equation below [35]:

$$\frac{1}{\tau_{corr}} = \frac{1}{\tau_{bulk}} + \frac{2J_{0e}(N_D + \Delta n)}{qWn_i^2} \tag{2}$$

where τ_{corr} is the Auger-corrected effective lifetime, τ_{bulk} is the bulk lifetime, J_{0e} is the emitter recombination factor [36], N_D is the base doping, Δn is the excess carrier density, q is the elemental charge, W is the wafer thickness and n_i is the intrinsic carrier density.

3. Results and discussion

3.1. Surface characteristics

The SEM images of the sample surfaces, shown in Fig. 2, demonstrate the fundamental physical differences between the RIE formed needle-shaped nanostructures and the chemically etched upright random pyramids. Note the different scales used for the SEM images. The wavelength dependent reflectance of the front surfaces, shown in Fig. 3, highlights the optical advantage of the nanostructured texture, which has less reflectance at all wavelengths, despite the incorporation of an additional anti-reflection coating on the random pyramid sample. The superior optical properties of RIE texture results in a gain of 0.64 mA/cm^2 photogenerated current over the Rp texture, under the AM 1.5G spectrum from 300 nm to 950 nm. The difference is expected to be bigger if the parasitic absorption within the SiN$_x$ film on Rp texture is taken into account. Note however that for photovoltaic applications some of this lost light will be trapped and reflected back onto the cell by the encapsulation layers in a module.

Surface statistics extracted from the AFM scans (Table 1) quantify the differences in surface topography. As expected, both σ_{rms} and τ_L are significantly higher for random pyramid textures compared to the RIE nanotextures. Note that this may have implications for the scattering of light from the nanotexture [37]. The effective slope index, expressed as the ratio between σ_{rms} and τ_L [38], and the peak angle (θ_{peak}) were far greater for the nanotexture. This results in the f_{surf} of the nanotexture being ~3 times higher than that of the random pyramid sample. Later in the paper we will demonstrate some correlation between this ratio, the enhancement in emitter doping and the amount of recombination within the doped texture regions. It is also worth noting that the random pyramid texture exhibits two dominant peaks in surface angle at 47° and 50°. This result is in good agreement with the literature and smaller than the common misconception of the pyramid angle being 54.7°, which assumes the texture as an ideal {111} bound pyramid resulted by the
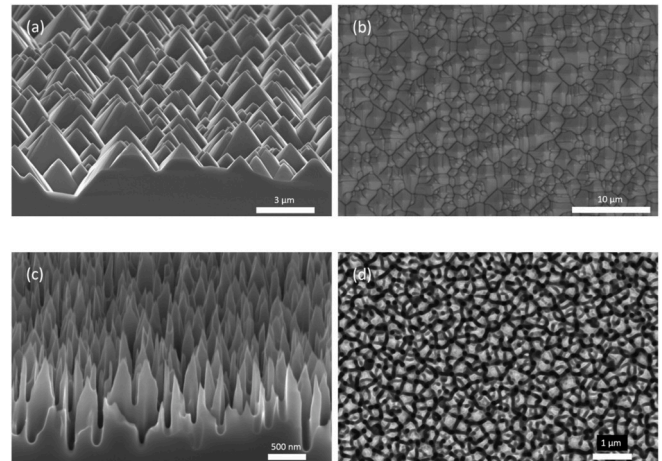

Fig. 2. Tilted (75°) and top view SEM images for random pyramid texture (a and b) and RIE nanotexture (c and d).
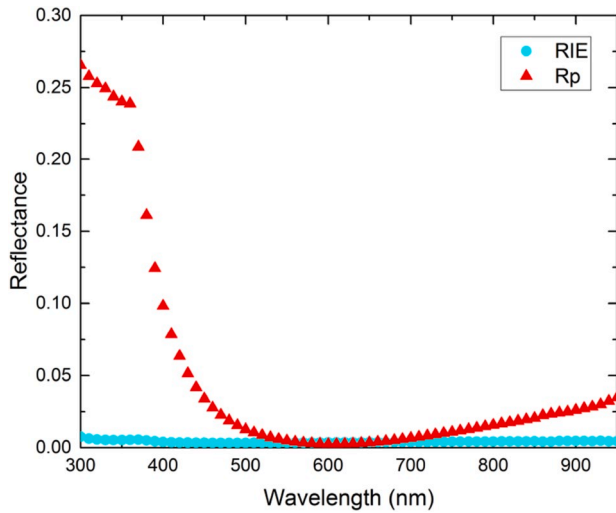
Fig. 3. Front surface reflectance of silicon nitride coated random pyramid texture and uncoated (bare silicon) RIE nanotexture from 300 nm to 950 nm. (For interpretation of the references to colour in this figure legend, the reader is referred to the Web version of this article.)

Table 1
Surface characteristics of random pyramid (RP) and reactive-ion etching (RIE) texture.

Texture	σ_{rms} (nm)	τ_L (nm)	σ_{rms}/τ_L	Θ_{peak} (°)	f_{surf}
Rp	481	1213	0.39	47, 50	1.44
RIE	224	137	1.63	75	4.19

ratio of etch rate of {111} and {100} orientation being infinte [39,40]. As a result, the measured surface area enhancement factor (f_{surf}) of the random pyramid is about 1.44 instead of 1.7.

3.2. Electrical properties

The front surface of a solar cell must provide adequate lateral conduction of majority carriers, limit the amount of recombination of minority carriers (at both open-circuit and short-circuit conditions) and provide good ohmic contact to metal contacts. In general, the ideal front surface would have a low sheet resistance and exhibit very low recombination (low J_{0E} and high collection efficiency). However, it is necessary to make a trade-off since the high doping concentration required to minimise resistive loss also results in higher recombination [22,41]. In this section we examine the first two of these and demonstrate processing that improves the performance of the nanotexture.

3.2.1. Impact of in-situ oxidation on the emitter doping

Increased oxygen concentration during diffusion resulted in increased sheet resistance (i.e. lighter doping) for all samples (see Fig. 4). This is consistent with the results seen in other studies utilising oxygen during drive-in Ref. [20]. In the case of the nanotexture a much higher O_2 concentration was required to reach the desired R_{sh} range (100 $\Omega/\square$ – 140 $\Omega/\square$) and for any specific oxygen concentration the doping was enhanced by the nanotexture. This enhancement is likely related to the increased surface area of the nanotexture (i.e. the increased f_{surf} shown in Table 1) which provides much more silicon per unit volume for the deposited phosphosilicate glass (PSG) to react with. This results in an increased release of P atoms as well as overall more source being provided by the increased surface area. Beyond 3% oxygen concentration the change in sheet resistance begins to flatten out. Given this was observed on both polished samples and nanotextured samples it is more likely related to a process limitation (e.g. the oxide thickness
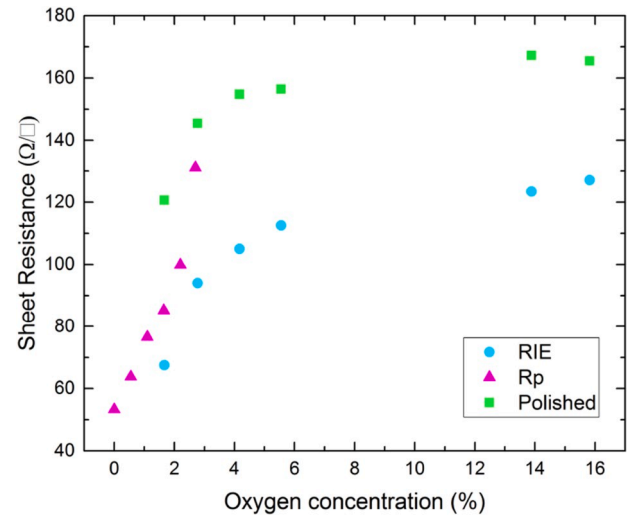

Fig. 4. Effect of in-situ oxidation during drive-in step on the sheet resistance of different textures.

may limit the supply of P). From the point of view of resistive loss, it would be better to have an emitter with lower sheet resistance, however the next section will demonstrate that these higher sheet resistance emitters provide more benefit through lower recombination than they lose through less conductivity.

Further insight into the junction formation on the different textured surfaces is revealed by means of cross-sectional SEM dopant contrast imaging (SEMDCI) of the post-diffusion nanotextured and Rp samples (Fig. 5). SEMDCI relies on a reduced acceleration voltage during SEM imaging, which causes phosphorous-doped regions to appear darker while boron-doped regions appear brighter [42–45]. Although the regions with highest contrast in the images have been shown to be correlated to the junction depth, the exact position of the junction would need further calibration [45]. Nevertheless, the relation between the surface topography and the dark regions are drastically different. On the random pyramid texture, the dark regions (i.e. emitter region) is conformal with the surface morphology. This results in a uniform junction depth (from the surface) and the centre volume of the pyramid remaining non-diffused. On the other hand, all the needles in the RIE texture appear dark and this extends into the region beneath the needles. This indicates that the entire volume of each needle is doped by phosphorous and that the electrical junction is formed in a somewhat parallel plane below the surface. This results in a non-uniform junction depth, with different points on the surface located at different distances from the junction.

The reason for the formation of different junction depths may be explained by considering the details of the diffusion process. During thermal diffusion, a PSG layer is deposited conformally on the nanotexture and as a result, phosphorus atoms are introduced into the needles from all sides. The junction depth of >400 nm is larger than the width of the nanofeatures (~100 nm). Therefore, phosphorus atoms diffusing from one side of the needles are expected to reach the other side and cause enhanced doping throughout the needles. Yet, no substantial contrast was observed within the nanowire as compared to deeper in the bulk. This observation could be limited by the imaging parameters used in the SEMDCI technique, which requires further optimization and studies. Nevertheless, the PSG deposited in the valleys introduces dopant down to the bulk of the silicon forming a rather homogeneously doped region underneath the RIE textures (appearing as a dark layer in the SEMDCI image). In contrast, the τ_L of the Rp texture is much larger than the junction depth. Therefore, no enhanced-doping effect is observed at the centre of the pyramids. It should be noted that an enhanced doping effect has been observed at the tips of Rp
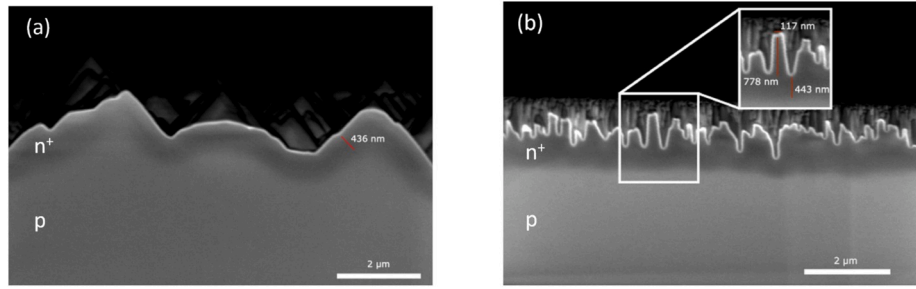
Fig. 5. Cross-sectional SEM doping contrast images for **(a)** random pyramid sample and **(b)** RIE sample. The phosphorus-diffused region appears darker whilst the boron-doped region appears brighter.

texture [46], however the total volume of those regions is not great and therefore is not expected to have any significant impact on overall doping.

The implications of this difference in junction formation on solar cell performance is complex. On the one hand a smaller total junction area is good since it potentially minimises junction recombination. Under open circuit conditions the high recombination surface being located at a distance from the junction is also good since it allows the emitter profile to shield bulk carriers from recombining there. However, for short-wavelength photons there exists much longer distances between carrier generation and junction collection. This has implications for the collection of light absorbed in the needles, particularly at shorter wavelengths. Furthermore, it is likely that the total amount of dopants incorporated into the needles is enhanced since phosphorous atoms may enter from all sides [10,17,47]. This will result in higher surface concentration and higher doping concentration within the emitter, both of which will increase recombination in those regions.

3.2.2. Emitter recombination

In addition to emitter optimization via in-situ oxidation, further improvements were also made to the surface passivation by means of corona deposition of additional surface charge. It is challenging to accurately measure the exact amount of charge successfully deposited onto a nano-textured surface and as such the results presented in this section refer to the amount of charge generated by the corona tool. The reduction in emitter recombination factor (J_{0e}) for three nanotextured samples (spanning the range of emitter strengths) is shown in Fig. 6 (left). Initially the 67 $\Omega/\square$ emitter had the lowest recombination factor, whilst the 112 $\Omega/\square$ emitter had the highest with the 127 $\Omega/\square$ emitter positioned between them. This demonstrates the complex balance between doping induced recombination and shielding of carriers from surface recombination. In all cases the J_{0e} of the nanotextured emitters was reduced by the corona deposition of charge. Once this improvement saturated the emitter with the least amount of doping had the lowest J_{0e}

and the heaviest emitter was the highest. Similar behaviour was also observed for the set of polished reference samples: the J_{0e} for all samples was reduced with additional corona charge deposited (Fig. 6, right). Since the initial J_{0e} of the polished samples was much lower compared to the RIE samples, the improvement in J_{0e} as a result of corona deposition of charge was less prominent. In addition, the total amount of generated charge required for the polished samples to reach saturation of J_{0e} was significantly less compared to the RIE samples. This could be related to the difference in surface area between these two set of samples, which is further discussed in supplementary material. Nevertheless, the best performing J_{0e} achieved on the polished samples is close to value reported in the literature for an industrial high efficiency passivated emitter and rear cell with selective emitter (27 fA/cm^2 vs 31 fA/cm^2) [48]. This result highlights the quality of emitter formation and surface passivation employed in this work.

It is interesting to understand the roles of surface charges further since it clearly provides one path to further performance improvement. Unfortunately, in this experiment it is only possible to study the impact of generated charge (i.e. not deposited charge) onto the emitters. The impact on emitter recombination is convoluted by two effects, the first is the efficiency of the deposition itself (i.e. what fraction of generated charge remains on the surface) and secondly how the different emitter doping reacts to the deposition of that charge. The former effect has been discussed in more details in the supplementary section.

The impact of generated charge onto the emitter recombination factor of RIE samples are summarized in Fig. 7. The results reveal that the total reduction in J_{0e} increases as the emitter R_{sh} increases. Since all the nanotextured samples have the same dielectric layers and the corona charges were deposited in identical fashion, this difference in the J_{0e} reduction (ΔJ_{0e}) should be attributed to the difference in emitter doping density and the interaction of different surface charge with different surface doping concentration. When surface doping density reduces, additional corona charge on the dielectric layer can progressively cause more significant band-bending near the surface. This repels minority
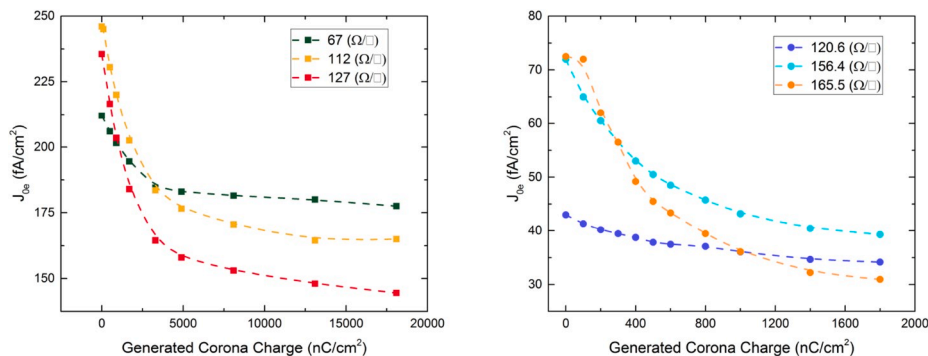

Fig. 6. Evolution of emitter recombination factor under corona charge deposition for reactive-ion etched silicon samples **(left)** and polished reference samples **(right)**. The dash lines serve as a guide to the eye. (For interpretation of the references to colour in this figure legend, the reader is referred to the Web version of this article.)
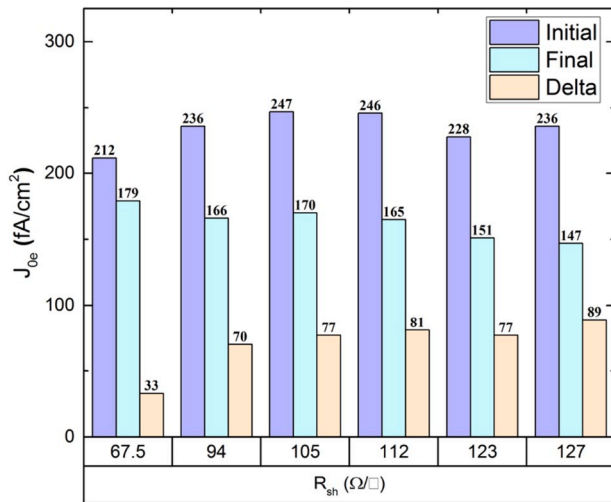
Fig. 7. Effect of corona charge deposition on the emitter recombination factor of RIE samples with different emitter sheet resistance.

carriers away from the trapping sites at the silicon/dielectric interface and hence surface recombination reduces. As a result, the larger reduction in J_{0e} through corona charging for the nanotextured samples with higher R_{sh} may be explained by the enhanced field effect passivation on the surface in combination with the reduction in emitter recombination due to less doping concentration. As a result, the final J_{0e} reduces with increasing R_{sh}, reaching 147 fA/cm^2 for a 127 $\Omega/\square$ emitter formed on reactive-ion etched surface.

The best values of emitter recombination factor (J_{0e}) measured on the nanotextures is shown in Fig. 8 (left). The heaviest emitter doping of ~65 $\Omega/\square$ had a J_{0e} of 179 fA/cm^2 which was then progressively reduced via in-situ oxidation to 147 fA/cm^2 for the ~127 $\Omega/\square$ emitter. Comparison to previous results in the literature (Fig. 8, right) demonstrates this to be a significant improvement compared to previous studies with the J_{0e} roughly halved for similar levels of sheet resistance. The selected literature data were chosen from studies that also employed deep RIE textures (weighted reflection less than 1%) with nominally the same ALD passivation stack as used in this study. It should be noted that [P] ion implantation was used in Van De Loo et al. and gas-phase diffusion was used in Pasanen et al. [17,49]. The J_{0e} improvement achieved in this work is attributed to the reduction in doping concentration both at the surface and within the bulk of the emitter on the nanotextured samples. These reduced doping levels also allowed the deposition of surface charge to play a greater role in reducing the overall recombination within the emitters. Compared to the J_{0e} measured on the random pyramid sample with similar R_{sh} (~130 $\Omega/\square$) there was a factor of ~3 for the best performing RIE sample. This has an interesting similarity to

the surface area ratio between these two textures, which may indicate that the surface area remains critical for the conditions investigated in this study. For the polished reference samples, the J_{0e} after corona deposition of charge remains relatively unchanged irrespective to different strength of emitters.

3.2.3. Carriers collection

The reduction in emitter recombination demonstrated above was also found to result in an improvement in the collection of carriers. Under short-circuit conditions, carriers generated within the emitter region must diffuse to the junction and be collected to contribute to the light generated current. Measurement of the normalised external quantum efficiency (EQE$_{PL, norm}$) of the nanotextured and Rp samples (Fig. 9, left) demonstrates in both cases an improvement with reduced sheet resistance. In the case of the nanotexture the EQE$_{PL}$ at 365 nm improved from 0.24 to 0.42 by increasing R_{sh}. It should be noted that this result is normalised to the performance at 660 nm and any absolute reduction there would result in an overall reduction in the absolute amount of carrier collection. Comparison to the RP sample reveals that there remains further scope for improvement. The random pyramid samples EQE$_{PL}$ (0.64–0.74) is superior to the nanotexture despite being reduced by the sub-optimal reflection and parasitic absorption within the SiN layer. The internal collection efficiency of these samples is 0.8–0.95 which is common in finished solar cells [20]. The nanotextured samples do not have parasitic absorption in any surface layers and it is likely the reduced EQE$_{PL}$ is the result of the deep junction, as shown in the SEMDCI image of Fig. 5. Under illumination, carriers generated at the valleys of the RIE texture need only travel 400 nm to be collected (similar to the distance in the RP sample). However, carriers generated within the needles need to travel an extra distance (up ~ 800 nm further) before reaching the junction. In addition, these needle regions are more heavily doped, and carriers must travel within 60 nm of the silicon surface where they are exposed to the trapping sites at the silicon/dielectric interface. Since the absorption depth for photons with 500 nm wavelength is about 1 μm, photons with shorter wavelengths were mainly absorbed within the needles. As a result, the generated carriers from short wavelength were strongly influenced by the geometry of the nano-scaled needles and its interaction with thermal diffusion described above. This result highlights collection efficiency as a key metric for the performance of nanotextures and one that should be considered during further optimization. The application of contact-less PL techniques provides a very useful means of measuring this on samples with extreme textured features where the formation of contact schemes may be difficult to achieve and/or may complicate the result.

4. Conclusion

In this paper, the electrical properties of emitters formed on RIE nanostructures were investigated and compared to upright random
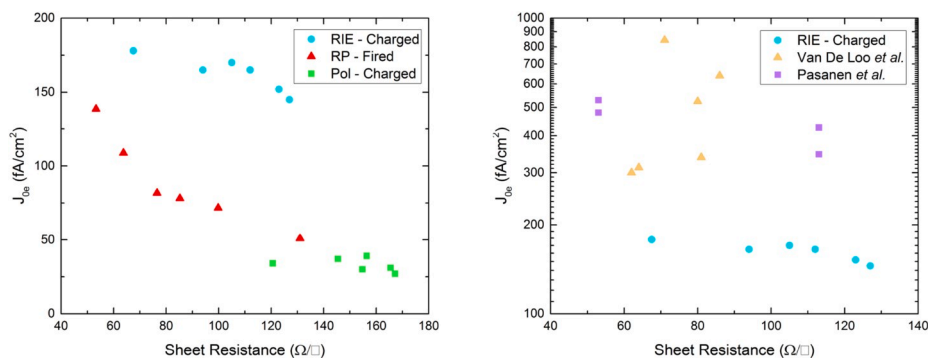

Fig. 8. (left) The best emitter recombination factor for RIE samples with different sheet resistance after saturation with corona charging, **(right)** Summary of emitter recombination for RIE samples and random pyramid samples fabricated in this paper and RIE samples reported in the literature [17,49].
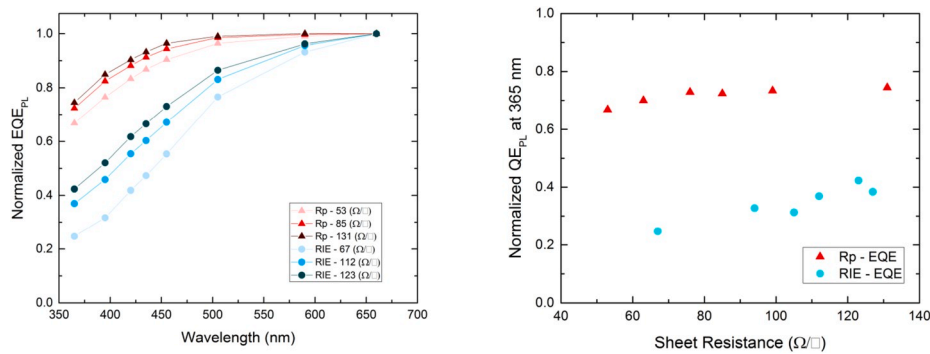
Fig. 9. (left) EQE_{PL} for random pyramid samples and RIE smaples as a function of illumination wavelength. **(right)** QE_{PL} at 365 nm for random pyramid samples and RIE samples with different sheet resistance.

pyramid samples. Emitter sheet resistance (R_{sh}) on the nanotextured samples ranging from 67 to 127 $\Omega/\square$ were achieved by adjusting the oxygen concentration during the drive-in step. It was found that increased levels of oxygen were required to account for the increased doping caused by the additional surface area of the nanotexture. After applying ALD passivation layers and additional corona charge, the J_{0e} was found to reduce with increasing oxygen concentration, reaching 147 fA/cm^2 for a surface area enhancement factor of $\sim$4.2, representing a significant improvement compared to previous studies. This result highlighted the effectiveness of in-situ oxidation as a strategy to improve the emitter quality, particularly when forming a junction on deep RIE textures. It also highlighted the need for an ALD film with higher positive fixed charge density. The lowest J_{0e} achieved on deep RIE texture was found to be approximately three times higher than the random pyramid sample with similar R_{sh}. This factor is suggested to be correlated to the surface area ratio between these two textures, as confirmed by atomic force microscopy. The internal quantum efficiency (measured using photoluminescence-based techniques) of the deep RIE samples was also improved by increasing the strength of in-situ oxidation process. Further scope for improvement was identified since values extracted were significantly lower than the random pyramid samples. Cross-sectional SEMDCI images revealed that the interaction between nano-scaled texture and thermal diffusion process causes doping throughout the whole RIE needles. It is suggested that the increased travel distance before being collected by the electrical junction combined with the higher exposure to the trapping sites within the needles, are responsible for the reduced collection efficiency within the emitter formed on deep RIE samples.

Declaration of competing interest

The authors declare that they have no known competing financial interests or personal relationships that could have appeared to influence the work reported in this paper.

CRediT authorship contribution statement

Tsun Hang Fung: Conceptualization, Methodology, Investigation, Writing - original draft. **Toni P. Pasanen:** Methodology, Investigation, Writing - original draft. **Yu Zhang:** Methodology, Investigation. **Anastasia Soeriyadi:** Methodology, Investigation. **Ville Vähänissi:** Methodology, Investigation, Writing - review & editing. **Giuseppe Scardera:** Methodology, Writing - review & editing. **David Payne:** Project administration, Funding acquisition. **Hele Savin:** Supervision, Project administration, Funding acquisition. **Malcolm Abbott:** Conceptualization, Supervision, Project administration, Funding acquisition.

Appendix A. Supplementary data

Supplementary data to this article can be found online at https://doi.org/10.1016/j.solmat.2020.110480.

References

[1] A. Ingenito, O. Isabella, M. Zeman, Nano-cones on micro-pyramids: modulated surface textures for maximal spectral response and high-efficiency solar cells, Prog. Photovoltaics Res. Appl. 23 (2015) 1649–1659, https://doi.org/10.1002/pip.2606.

[2] H. Savin, P. Repo, G. Von Gastrow, P. Ortega, E. Calle, M. Garín, R. Alcubilla, Black silicon solar cells with interdigitated back-contacts achieve 22.1% efficiency, Nat. Nanotechnol. 10 (2015) 624–628, https://doi.org/10.1038/nnano.2015.89.

[3] P. Zheng, J. Xu, H. Sun, F. Zhang, Y. Guo, H. Pan, K.S. Chan, J. Jin, H. Wang, W. Chen, X. Zhang, H. Jin, 21.63% industrial screen-printed multicrystalline Si solar cell, Phys. Status Solidi Rapid Res. Lett. 11 (2017) 1–4, https://doi.org/10.1002/pssr.201600453.

[4] S. Zhang, Y. Yang, D. Chen, W. Deng, H. Huang, P.P. Altermatt, J. Xu, Z. Feng, P. J. Verlinden, 19 . 86 % aperture efficient world record P - type multi - crystalline module with 20 . 59 % efficient PERC solar cells, in: 44th IEEE Photovolt. Spec. Conf, 2017.

[5] B. Meinel, T. Koschwitz, C. Blocks, J. Acker, Comparison of diamond wire cut and silicon carbide slurry processed silicon wafer surfaces after acidic texturisation, Mater. Sci. Semicond. Process. 26 (2014) 93–100, https://doi.org/10.1016/j.mssp.2014.03.046.

[6] F. Cao, K. Chen, J. Zhang, X. Ye, J. Li, S. Zou, X. Su, Next-generation multi-crystalline silicon solar cells: diamond-wire sawing, nano-texture and high efficiency, Sol. Energy Mater. Sol. Cells 141 (2015) 132–138, https://doi.org/10.1016/j.solmat.2015.05.030.

[7] J. Sheng, W. Wang, Q. Ye, J. Ding, N. Yuan, C. Zhang, MACE texture optimization for mass production of high-efficiency multi-crystalline cell and module, IEEE J. Photovoltaics 9 (2019) 918–925, https://doi.org/10.1109/JPHOTOV.2019.2896338.

[8] S. Zhong, B. Liu, Y. Xia, J. Liu, J. Liu, Z. Shen, Z. Xu, C. Li, Influence of the texturing structure on the properties of black silicon solar cell, Sol. Energy Mater. Sol. Cells 108 (2013) 200–204, https://doi.org/10.1016/j.solmat.2012.10.001.

[9] P. Li, Y. Wei, X. Tan, X. Li, Y. Wang, Z. Zhao, Z. Yuan, A. Liu, Effective optimization of emitters and surface passivation for nanostructured silicon solar cells, RSC Adv. 6 (2016) 104073–104081, https://doi.org/10.1039/c6ra20945a.

[10] B. Kafle, J. Schön, C. Fleischmann, S. Werner, A. Wolf, L. Clochard, E. Duffy, M. Hofmann, J. Rentsch, On the emitter formation in nanotextured silicon solar cells to achieve improved electrical performances, Sol. Energy Mater. Sol. Cells 152 (2016) 94–102, https://doi.org/10.1016/j.solmat.2016.03.031.

[11] X. Dai, R. Jia, G. Su, H. Sun, K. Tao, C. Zhang, P. Zhang, Z. Jin, X. Liu, The influence of surface structure on diffusion and passivation in multicrystalline silicon solar cells textured by metal assisted chemical etching (MACE) method, Sol. Energy Mater. Sol. Cells 186 (2018) 42–49, https://doi.org/10.1016/j.solmat.2018.06.011.

[12] M.M. Plakhotnyuk, M. Gaudig, R.S. Davidsen, J.M. Lindhard, J. Hirsch, D. Lausch, M.S. Schmidt, E. Stamate, O. Hansen, Low surface damage dry etched black silicon, J. Appl. Phys. 122 (2017), https://doi.org/10.1063/1.4993425.

[13] L. Sainiemi, V. Jokinen, A. Shah, M. Shpak, S. Aura, P. Suvanto, S. Franssila, Non-reflecting silicon and polymer surfaces by plasma etching and replication, Adv. Mater. 23 (2011) 122–126, https://doi.org/10.1002/adma.201001810.

[14] P. Repo, A. Haarahiltunen, L. Sainiemi, M. Yli-Koski, H. Talvitie, M.C. Schubert, H. Savin, Effective passivation of black silicon surfaces by atomic layer deposition, IEEE J. Photovoltaics 3 (2013) 90–94, https://doi.org/10.1109/JPHOTOV.2012.2210031.

[15] Y. Liu, T. Lai, H. Li, Y. Wang, Z. Mei, H. Liang, Z. Li, F. Zhang, W. Wang, A. Y. Kuznetsov, X. Du, Nanostructure formation and passivation of large-area black silicon for solar cell applications, Small 8 (2012) 1392–1397, https://doi.org/10.1002/smll.201101792.

[16] X. Liu, P.R. Coxon, M. Peters, B. Hoex, J.M. Cole, D.J. Fray, Black silicon: fabrication methods, properties and solar energy applications, Energy Environ. Sci. 7 (2014) 3223–3263, https://doi.org/10.1039/c4ee01152j.

[17] T. Pasanen, V. Vähänissi, N. Theut, H. Savin, Surface passivation of black silicon phosphorus emitters with atomic layer deposited SiO2/Al2O3stacks, Energy Procedia 124 (2017) 307–312, https://doi.org/10.1016/j.egypro.2017.09.304.

[18] T. Pasanen, Surface Passivation of Black Silicon Phosphorus Emitters, 2017. https://aaltodoc.aalto.fi/handle/123456789/24696.

[19] H. Li, F.J. Ma, Z. Hameiri, S. Wenham, M. Abbott, On elimination of inactive phosphorus in industrial POCl3diffused emitters for high efficiency silicon solar cells, Sol. Energy Mater. Sol. Cells 171 (2017) 213–221, https://doi.org/10.1016/j.solmat.2017.06.040.

[20] H. Li, B. Hallam, S. Wenham, M. Abbott, Oxidation drive-in to improve industrial emitter performance by POCl3 diffusion, IEEE J. Photovoltaics 7 (2017) 144–152, https://doi.org/10.1109/JPHOTOV.2016.2631300.

[21] D. Redfield, Mechanism of performance limitations in heavily doped silicon devices, Appl. Phys. Lett. 33 (1978) 531–532, https://doi.org/10.1063/1.90426.

[22] H. Wagner, A. Dastgheib-Shirazi, B. Min, A.E. Morishige, M. Steyer, G. Hahn, C. Del Cañizo, T. Buonassisi, P.P. Altermatt, Optimizing phosphorus diffusion for photovoltaic applications: peak doping, inactive phosphorus, gettering, and contact formation, J. Appl. Phys. 119 (2016), https://doi.org/10.1063/1.4949326.

[23] T.P. Pasanen, H.S. Laine, V. Vähänissi, J. Schön, H. Savin, Black silicon significantly enhances phosphorus diffusion gettering, Sci. Rep. 8 (2018) 1–6, https://doi.org/10.1038/s41598-018-20494-y.

[24] S. Zhong, B. Liu, Y. Xia, J. Liu, J. Liu, Z. Shen, Z. Xu, C. Li, The study on the properties of black multicrystalline silicon solar cell varying with the diffusion temperature, Energy Procedia 14 (2012) 505–511, https://doi.org/10.1016/j.egypro.2011.12.966.

[25] B. Kafle, T. Freund, J. Schon, S. Werner, A. Wolf, A. Lorenz, P. Saint-Cast, L. Clochard, E. Duffy, M. Hofmann, J. Rentsch, On the nature of emitter diffusion and screen-printing contact formation on nanostructured silicon surfaces, IEEE J. Photovoltaics. 7 (2017) 136–143, https://doi.org/10.1109/PVSC.2017.8366872.

[26] R.S. Davidsen, H. Li, A. To, X. Wang, A. Han, J. An, J. Colwell, C. Chan, A. Wenham, M.S. Schmidt, A. Boisen, O. Hansen, S. Wenham, A. Barnett, Black silicon laser-doped selective emitter solar cell with 18.1% efficiency, Sol. Energy Mater. Sol. Cells 144 (2016) 740–747, https://doi.org/10.1016/j.solmat.2015.10.018.

[27] W. Kern, D.A. Puotinen, Cleaning solutions based on hydrogen peroxide for use in silicon semiconductor technology, RCA Rev. 31 (1970) 187–206.

[28] Z. Hameiri, N. Borojevic, L. Mai, N. Nandakumar, K. Kim, S. Winderbaum, Low-absorbing and thermally stable industrial silicon nitride films with very low surface recombination, IEEE J. Photovoltaics 7 (2017) 996–1003, https://doi.org/10.1109/JPHOTOV.2017.2706424.

[29] M. Wilson, J. Lagowski, L. Jastrzebski, A. Savtchouk, V. Faifer, COCOS (corona oxide characterization of semiconductor) non-contact metrology for gate dielectrics, AIP Conf. Proc. (2001) 220–225, https://doi.org/10.1063/1.1354401.

[30] R.A. Sinton, A. Cuevas, M. Stuckings, Quasi-steady-state photoconductance, a new method for solar cell material and device characterization, in: 25th IEEE Photovolt. Spec. Conf, 1996, pp. 457–460.

[31] A. Richter, S.W. Glunz, F. Werner, J. Schmidt, A. Cuevas, Improved quantitative description of Auger recombination in crystalline silicon, Phys. Rev. B 165202 (2012) 1–14, https://doi.org/10.1103/PhysRevB.86.165202.

[32] A. Paduthol, M.K. Juhl, T. Trupke, Correcting the effect of LED spectra on external quantum efficiency measurements of solar cells, IEEE J. Photovoltaics 8 (2018) 559–564, https://doi.org/10.1109/JPHOTOV.2017.2787022.

[33] A. Paduthol, M.K. Juhl, T. Trupke, Limitations of photoluminescence based external quantum efficiency measurements, Jounrnal Appl. Phys. 123 (2018) 1–8, https://doi.org/10.1109/PVSC.2018.8548179.

[34] D. Nečas, P. Klapetek, Gwyddion: an open-source software for SPM data analysis, Cent. Eur. J. Phys. 10 (2012) 181–188, https://doi.org/10.2478/s11534-011-0096-2.

[35] D.E. Kane, R.M. Swanson, Measurement of the emitter saturation current by a contactless photoconductivity decay method, in: 18th IEEE Photovolt. Spec. Conf, 1985, pp. 578–583.

[36] A. Cuevas, The recombination parameter J0, Energy Procedia 55 (2014) 53–62, https://doi.org/10.1016/j.egypro.2014.08.073.

[37] M. Steglich, T. Käsebier, M. Zilk, T. Pertsch, E.B. Kley, A. Tünnermann, The structural and optical properties of black silicon by inductively coupled plasma reactive ion etching, J. Appl. Phys. 116 (2014), https://doi.org/10.1063/1.4900996.

[38] M. Hollaus, M. Milenkovic, N. Pfeifer, A Review of Surface Roughness Concepts , Indices and Applications, 2014.

[39] E. Forniés, C. Zaldo, J.M. Albella, Control of random texture of monocrystalline silicon cells by angle-resolved optical reflectance, Sol. Energy Mater. Sol. Cells 87 (2005) 583–593, https://doi.org/10.1016/j.solmat.2004.07.040.

[40] S.C. Baker-finch, K.R. Mcintosh, Reflection distributions of textured monocrystalline silicon: implications for silicon solar cells, Prog. Photovoltaics Res. Appl. 21 (2013) 960–971, https://doi.org/10.1002/pip.

[41] R.R. King, R.A. Sinton, R.M. Swanson, Studies of diffused phosphorus emitters: saturation current, surface recombination velocity, and quantum efficiency, IEEE Trans. Electron. Dev. 37 (1990) 365–371, https://doi.org/10.1109/16.46368.

[42] P. Kazemian, A.C. Twitchett, C.J. Humphreys, C. Rodenburg, Site-specific dopant profiling in a scanning electron microscope using focused ion beam prepared specimens, Appl. Phys. Lett. 88 (2006), https://doi.org/10.1063/1.2207552.

[43] L. Xu, K. Weber, S.P. Phang, A. Fell, F. Brink, D. Yan, X. Yang, E. Franklin, H. Chen, Secondary electron microscopy dopant contrast image (SEMDCI) for laser doping, IEEE J. Photovoltaics 3 (2013) 762–768, https://doi.org/10.1109/JPHOTOV.2013.2241820.

[44] Y. Komatsu, D. Harata, E.W. Schuring, A.H.G. Vlooswijk, S. Katori, S. Fujita, P. R. Venema, I. Cesar, Calibration of electrochemical capacitance-voltage method on pyramid texture surface using scanning electron microscopy, Energy Procedia 38 (2013) 94–100, https://doi.org/10.1016/j.egypro.2013.07.254.

[45] J.T. Heath, C.S. Jiang, M.M. Al-Jassim, Imaging the solar cell P-N junction and depletion region using secondary electron contrast, Conf. Rec. IEEE Photovoltaics Spec. Conf. (2011) 1656–1661, https://doi.org/10.1109/PVSC.2011.6186274.

[46] H. Wagner, S. Steingrube, B. Wolpensinger, A. Dastgheib-Shirazi, R. Chen, S. T. Dunham, P.P. Altermatt, Analyzing emitter dopant inhomogeneities at textured Si surfaces by using 3D process and device simulations in combination with SEM imaging, Conf. Rec. IEEE Photovolt. Spec. Conf. (2012) 313–316, https://doi.org/10.1109/PVSC.2012.6317625.

[47] J. Oh, H.-C. Yuan, H.M. Branz, An 18.2%-efficient black-silicon solar cell achieved through control of carrier recombination in nanostructures, Nat. Nanotechnol. 7 (2012) 743–748, https://doi.org/10.1038/nnano.2012.166.

[48] A. Fell, P.P. Altermatt, A detailed full-cell model of a 2018 commercial PERC solar cell in Quokka3, IEEE J. Photovoltaics 8 (2018) 1443–1448, https://doi.org/10.1109/JPHOTOV.2018.2863548.

[49] B.W.H. Van De Loo, A. Ingenito, M.A. Verheijen, O. Isabella, M. Zeman, W.M. M. Kessels, Surface passivation of n -type doped black silicon by atomic-layer-deposited SiO 2/Al 2 O 3 stacks, Appl. Phys. Lett. 110 (2017), https://doi.org/10.1063/1.4989824.